Article

Realization of a non-markov chain in a single 2D mineral RRAM

Rongjie Zhang [a,1], Wenjun Chen [a,1], Changjiu Teng [a], Wugang Liao [b], Bilu Liu [a,*], Hui-Ming Cheng [a,c,*]

[a] Shenzhen Geim Graphene Center, Tsinghua-Berkeley Shenzhen Institute and Institute of Materials Research, Tsinghua Shenzhen International Graduate School, Tsinghua University, Shenzhen 518055, China
[b] Institute of Microscale Optoelectronics, Shenzhen University, Shenzhen 518060, China
[c] Shenyang National Laboratory for Materials Science, Institute of Metal Research, Chinese Academy of Sciences, Shenyang 110016, China

A B S T R A C T

The non-Markov process exists widely in thermodymanic process, while it usually requires the packing of many transistors and memories with great system complexity in a traditional device structure to minic such functions. Two-dimensional (2D) material-based resistive random access memory (RRAM) devices have the potential for next-generation computing systems with much-reduced complexity. Here, we achieve a non-Markov chain in an individual RRAM device based on 2D mineral material mica with a vertical metal/mica/metal structure. We find that the potassium ions (K^+) in 2D mica gradually move in the direction of the applied electric field, making the initially insulating mica conductive. The accumulation of K^+ is changed by an electric field, and the 2D-mica RRAM has both single and double memory windows, a high on/off ratio, decent stability, and repeatability. This is the first time a non-Markov chain process has been established in a single RRAM, in which the movement of K^+ is dependent on the stimulated voltage as well as their past states. This work not only uncovers an intrinsic inner ionic conductivity of 2D mica, but also opens the door for the production of such RRAM devices with numerous functions and applications.

1. Introduction

Information technology plays an increasing important role in human society while conventional von-Neumann architecture is approaching its limit when processing the exponentially growing amount of data [1,2]. Combining memory/sensor cells and algorithms into cutting edge hardware and devices [3] is important in next-generation computing [4,5]. To this end, resistive random access memory (RRAM) or memristors [6,7] have been proposed to complement traditional non-volatile memory devices because of their high operation speed, high integration density, as well as applications in complex algorithms [8–11]. Recently, two-dimensional (2D) materials have emerged as a versatile platform for RRAM applications [12–17]. Compared with bulk materials, the RRAMs based on 2D materials have an outstanding performance. For example, 2D material-based RRAMs have shown ultra-fast switching of <10 ns [18], the thinnest nonvolatile resistive switching (RS) [19], a sub-pA switching current [20], an ultra-low operation voltage of 100 mV [21], high-frequency operation at

GHz level [22], and excellent stability at high temperature of up to 340 °C [23].

The high integration of RRAMs is advantageous to accomplish specific functional algorithms in a machine learning system. Although deep learning algorithms can be realized by software, numerous transistors are usually needed [24], which may degrade the operation stability and robustness of the system. Several algorithms, such as sparse coding, convolution neural network and reinforcement learning, are accomplished by using RRAM arrays [25–30]. The use of RRAM arrays requires software and hardware assistance. To overcome these limitations, a Markov chain, which is usually realized by software, was achieved in a single RRAM based on 2D SnSe [31]. The Markov chain simplifies and reduces the calculation in the system, and shows great potential in machine learning and automatic speech recognition. However, various physical phenomena are related to the non-Markov [32] property, where the probability of the next state is related to both current and past states. For instance, a Markov chain is not applicable in the systems which are related to their historical states, such as time-dependence human neural memory brain, environmental-related quantum entangled state [33], and cumulative effect, etc. The achievement of a hardware non-Markov chain is elusive as it refers to complicated process, which hindrads the application of the non-Markov process in historically related

physical processes. In addition, a vacancy-based or external ion based RS mechanism may cause the variation of RRAM performance, such as random telegraph noise [34] and set voltage variability [35], which is challenging to address. Therefore, it is urgent to explore new RS mechanisms to achieve a non-Markov process with high performance.

Here, we report the realization of a non-Markov chain in a single 2D crystal RRAM with an intrinsic internal ionic conduction mechanism. We find that the migration of the internal K^+ in 2D mica leads to the formation of conductive filament (CF) paths, which is comfirmed by electrical measurements and a depth anylysis of K^+ distribution. The 2D mica RRAM exhibits both single and double memory windows with a high on/off current ratio of 10^3, high stability and repeatability, verified by conductive atomic force microscopy (CAFM) measurements. The mica-based RRAM is capable of remembering the polarity of input voltages, resulting in the different response behaviors of K^+ in mica under positive and negative electrical fields. As a result, a non-Markov process has been realized in an individual RRAM for the first time. The internal ion transport demonstrated in this paper provides additional dimensions in memory devices, opening a new way for the design and fabrication of intelligent devices.

2. Experimental

2.1. Device fabrication

For the mica-based RRAM, a Cr/Au (5 nm/50 nm) film was deposited on a 300 nm-thick-SiO_2/Si substrate by an e-beam evaporation system (TSV-1500, Tianxingda Vacuum Coating Equipment Co. Ltd., China). Mica flakes were mechanically exfoliated using Scotch tape from the commercial bulk material (HQ graphene, Nederland) and directly transferred onto the Cr/Au-coated substrate.

Fabrication of probe/potassium iodide (KI) solution/mica/Au devices: first, photoresist (PR) (AZ 5214) was spin-coated (2000 r/min) to cover the whole substrate, followed by baking the sample on a hot plate at 125 °C for 1 min. Second, the shape of the bottom Au electrode was defined by a laser writer system (Dall, Aresis, Slovenia), followed by Au deposition using an e-beam evaporation system. Third, the mica was mechanically exfoliated using Scotch tape and transferred onto the bottom Au electrode with the assistance of polydimethylsiloxane (PDMS) using a homemade alignment station. Forth, another layer of PR was spin-coated and baked in the substrate. Fifth, laser writing was used to ablate a hole in the PR layer as a window to expose the mica flake to air. For device testing, a droplet of KI/DI water solution was dropped into the window.

Fabrication of graphite/mica/graphite and mica/MoS_2/graphite devices: first, the graphite (HQ graphene), muscovite mica (HQ graphene), fluorophlogopite mica (Tiancheng Fluor phlogopite Mica Co., Ltd., China) and MoS_2 (HQ graphene) flakes were exfoliated using Scotch tape from bulk crystals onto PDMS and identified by an optical microscope. Second, a target 2D flake was affixed on a SiO_2 (300 nm)/Si substrate in a homemade alignment station with the assistance of PDMS. Third, PR was spin-coated (2000 r/min) to cover the whole substrate and baked on a hot plate (125 °C, 1 min). Forth, the electrodes were fabricated by a laser writer system and an e-beam evaporation system.

2.2. Electrical measurements

AFM characterization and CAFM measurements were performed by AFM (Cypher ES, Oxford Instruments, UK). For all the CAFM measurements, a fixed compliant current of 10 nA was used.

Performance testing of the devices based on KI solution and graphite/mica/graphite was performed using a probe station, and the relevant current-voltage (*I-V*) curves were collected by a semiconductor parameter analyzer (Keithley 4200, USA).

2.3. The TOF-SIMS measurements

The time-of-flight secondary-ion mass spectrometry (TOF-SIMS) depth profiles were obtained on a TOF-SIMS 5-100 instrument (IONTOF, Münster, Germany) equipped with a 30-keV Bi_3^+ liquid metal ion source for analysis and a 1-keV Cs^+ source for sputtering. Both sources stuck the sample surface at an angle of 45°. MCs^+ mode measurements were carried out to detect both MCs^+ ions (M is K, Al, Si, Au, Cr) and MCs_2^+ (M is C, O) with analysis beam current of 0.7 pA and sputter beam current of 40 nA. The analysis area and sputter area were 15 μm × 15 μm and 200 μm × 200 μm, respectively. To achieve a better charge compensation during measurements, an electron flood gun and a non-interlaced scans mode were used.

3. Results and discussion

Fig. 1a shows the structure and measurement schematics of the RRAM based on 2D mica, in which the AFM tip is an electrode to apply voltage and the bottom Au electrode is Au. The application of an electric field leads to the accumulation of K^+ along the direction of the electrical field, which forms a CF in the vertical direction of mica (Fig. 1b). Here, trilayer mica with a thickness of 3 nm is selected to reveal the RS behavior. Fig. 1c shows the optical image of the mica flake whose thickness was determined by AFM (inset of Fig. 1d). The *I-V* curves (Fig. 1e) show that the mica-based device is initially insulating then conductive under the application of a cyclic triangular wave voltage with the maximum value of 2 V. The typical RRAM window is observed after 30 cycles, representing the formation of CF in the device. The mica is initially insulating (with a resistance >10 GΩ), and gradually switches to a low resistance state (<0.1 GΩ) at a positive voltage of 1.5 V. The formation of CF results in the formation of a stable RRAM window with a width of 0.8 V in the following sweeps. When the amplitude of the voltage is increased to 4 V, the mica shows stable bipolar RRAM characteristics with 1.5 V windows after 10 cycles (Fig. 1f), indicating the easier formation of the CF in mica under a higher electrical field. In contrast to the traditional RRAM with either unipolar or bipolar windows, the mica-based device uniquely shows single and double memory windows, the transformation between which can be simply made by controlling the intensity of the applied electric field. This tunable RRAM behavior makes 2D mica useful in functional devices. For example, RRAM with a single memory window can be seen as the selector in crossbar electronics. In addition, the changeable behavior between single and double memory windows in a single device is advantageous for oscillation sources.

The accumulation and migration of K^+ driven by an electric field reveal the conductive behavior of mica. To verify the electrodialysis ability of K^+ in mica, a device based on aqueous KI/mica/Au with free K^+ was fabricated (Fig. 2a). In detail, a layer of PR was spin-coated and dried to cover the whole substrate. Then a hole was made in the PR layer by laser ablation to act as a window to allow external K^+ offered by the KI/DI water solution to move through the mica (see details in Experimental). The *I-V* curves of the device with one probe attached to the bottom Au electrode (ground) and another immersed in a droplet of KI solution, were measured in air. As shown in Fig. 2b, the KI/mica/Au device was initially at a high-resistance state (>1 GΩ), and changed to a low-resistance state (<200 kΩ) after the application of a positive voltage with a maximum value of 20 V. The reason for this is that the K^+ in KI
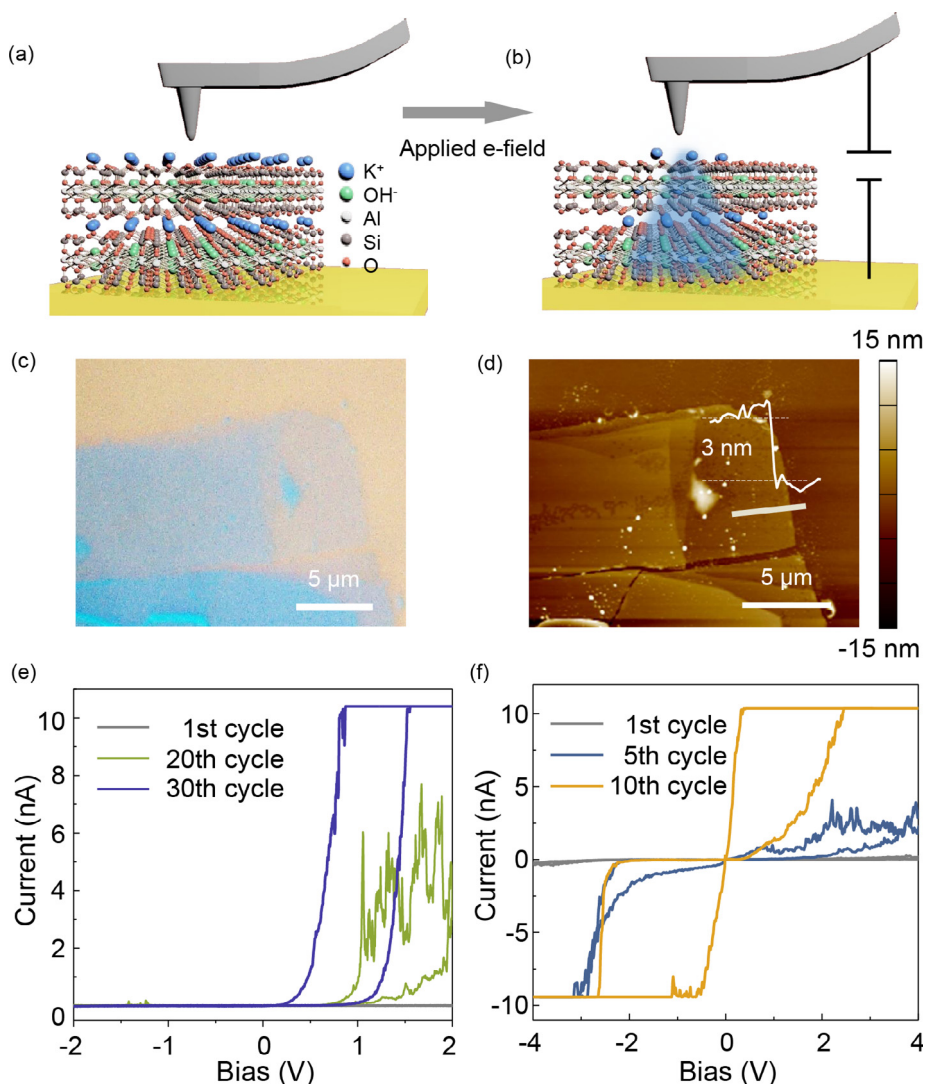
Fig. 1. Device structure and electrical characteristics of a 2D-mica-based RRAM. Schematic of the distribution of K^+ in the device (a) before and (b) after the application of a positive electric field. (c) Optical microscope image of 2D mica on a Au/SiO$_2$/Si substrate. (d) AFM image of the thin-layer mica in (c). Inset is the height analysis of the mica, showing its thickness of ~3 nm. (e) The 1st, 10th, and 30th RS characteristics of the mica-based device at a cyclic triangular wave voltage of amplitude 2 V. (f) The 1st, 5th, and 10th RS characteristics of the mica-based device at a cyclic triangular wave with an amplitude of 4 V.

solution gathers at the top of mica and then gradually migrates through the mica $Al_2(AlSi_3O_{10})(OH)_2^-$ layer which causes the conduction. To confirm the migration mechanism of K^+, a pulse voltage (±2.5 V) was used to stimulate the KI/mica/Au device after the formation of CF. A clear current vibration at a voltage of 1 V is seen in 150 pulse cycles (Fig. 2c). The conductivity of the KI/mica/Au device decreases under the negative pulse voltage, since the K^+ is forced to return to the top layer of mica. In contrast, the device becomes more conductive under a positive voltage because of the continuous accumulation of K^+. The results show that the external K^+ can migrate in the out-of-plane direction of the mica under an electrical field.

In addition to the external K^+, the accumulation and rearrangement of the internal K^+ of mica also contribute to the RS behavior. The different electrical features of transistors based on MoS$_2$/muscovite mica and MoS$_2$/fluorphlogopite mica confirm the migration of internal K^+ in the mica (Figs. S1 and S2 online). Another device based on a stacked graphite/mica/graphite structure (Fig. S3a online) was fabricated to rule out the possibility of the formation of the CF from the electrodes. Fig. S3b (online) shows a similar RRAM window of the graphite/mica/graphite device. It is known that the carbon atoms in graphite are immovable under the electri-

cal field because of the strong covalent bonds. From all the above results, we conclude that the vertical conduction of mica is ascribed to the movement of its internal ions.

Next, we analysis the conduction mechanism of the device by examing the concentrations of K^+ at different stages. We use TOF-SIMS, a common technique for the depth profiling of materials [36,37], to explore the migration of K^+ in mica. Here, we study the graphite/mica/graphite structure (Fig. 2d) with TOF-SIMS. Fig. 2e shows the profiles of C, Si, K, and Al elements as a function of depth in the device. The two separate regions of C signal correspond to the top and bottom graphite, between which the Si, K, and Al signals belong to the mica layer sandwiched by two graphite electrodes. Before the application of a voltage, the intensity of K remains nearly constant, suggesting the homogeneous distribution of K^+ in mica. After the application of a positive vertical voltage (Fig. 2f), the increasing gradient of K profile reflects the movement of K^+ from the top of mica to the bottom, as illustrated in Fig. 2a. In contrast, the C signals in the two devices show the same increasing and decreasing trend. In addition, the TOF-SIMS signals of the device based on Au/Cr/mica/Au/Cr in Fig. S4 (online) also indicate the same increasing amount of K^+ after the application of an electric field. Therefore, the TOF-SIMS analyses show that the
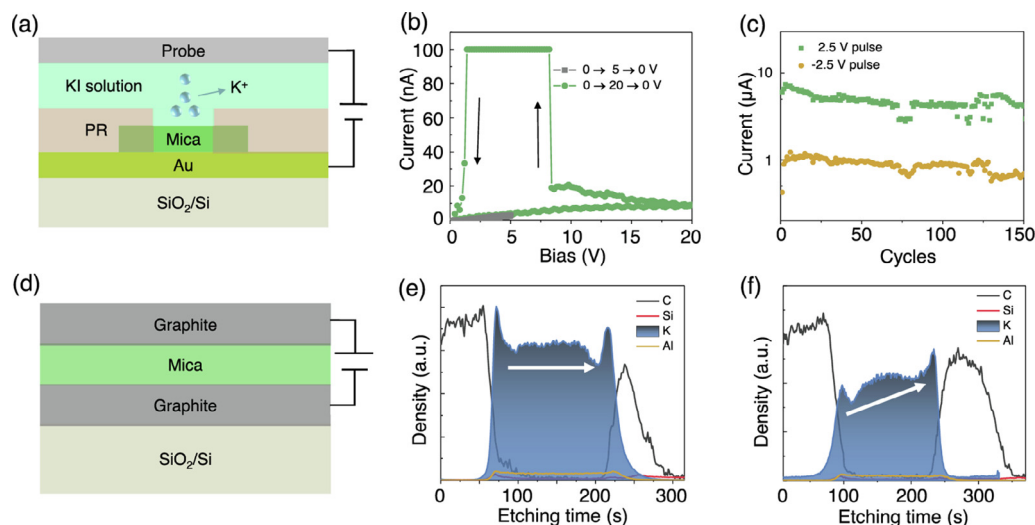
Fig. 2. K$^+$ transport along the vertical direction in 2D mica. (a) Schematic of the probe/KI solution/mica/Au device for the measurements of K$^+$ transport. RS characteristics (b) of the device in (a). (c) The current in a read voltage of 1 V of the device in (a) after the application of voltage pulses (±2.5 V). (d) Schematic of the graphite/mica/graphite device. The TOF-SIMS depth profiling of C, Si, K, and Al elements in graphite/mica/graphite (e) without and (f) after the application of a positive voltage. The thicknesses of mica flakes in devices (e) and (f) are comparable owing to the similar etching time.

conduction of mica in the out-of-plane direction mainly relies on the migration of K$^+$ under an electrical field, although some other factors may exist that contribute to the switching behaviors in 2D-mica. The above KI, MoS$_2$ FETs, graphite/mica/graphite, and SIMS analysis together suggest that the internal K$^+$ transport plays a key role in the RS of 2D mica devices.

The unique RRAM behavior in 2D-mica-based devices can be understood by the migration of K$^+$ under an electrical field. Fig. 3a shows the counterclockwise single RRAM window of the device produced by a cyclic triangular wave voltage with an amplitude of 2 V. Note that the single memory window is transformed to a clockwise double memory window when the amplitude of the periodic voltage is increased to 5 V (Fig. 3b). The formation of two distinct RRAM windows is mainly attributed to the voltage scanning in different ranges. Fig. 3c shows the dynamics of K$^+$ after the device was stimulated by a triangular wave voltage with an amplitude of 2 V. The K$^+$ from the top layer of mica pass through the Al$_2$(AlSi$_3$O$_{10}$)(OH)$_2^-$ layer under the 0 to 2 V voltage sweep. The local accumulation of K$^+$ enables the conduction of mica, which causes the increasing current in the vertical direction of mica. The subsequent positive electric field (2 to 0 V sweep) continuously motivates the gathering of the positive ions. Thus, the mica is more conductive at this stage than the former, resulting in the RRAM window. Note that the accumulated K$^+$ is returned to the initial position immediately when the electrical field is changed to negative, which returns the mica to the insulation state. Consequently, the device shows a single RRAM window under an increasing voltage sweep from –2 to 2 V. In contrast, in the case of higher electrical field (cyclic triangular wave voltage sweep with the amplitude of 5 V), the mica-based RRAM shows a bipolar behavior, the mechanism of which is illustrated in Fig. 3d. The higher negative voltage reverses the arrangement of K$^+$ compared to the positive electrical filed. The accumulation of K$^+$ also connects the two electrodes, contributing to the conduction of mica. As a result, the mica-based RRAM has a low resistance state in 0 to 5 V sweep. The accumulation of K$^+$ would gradually disperse under the positive electrical field, which provides enough energy to return the mica to its original insulation state. This makes the device exhibit a clockwise RRAM window for positive voltage. From 0 to –5 V sweep, the K$^+$ slightly re-accumulates under the higher electrical field. Further application of a negative voltage produces a higher current in the mica than before with the increasing accumulation of K$^+$, leading

to the RRAM window for a negative voltage. In brief, the K$^+$ in mica migrate through the Al$_2$(AlSi$_3$O$_{10}$)(OH)$_2^-$ layer under an electrical field, forming the CF in the mica-based RRAM. The different accumulation directions of K$^+$ under a positive or a negative electrical field contribute to single or double RRAM windows in the mica-based RRAM.

Besides RRAM windows, the repeatability and on/off ratio are two important criteria to evaluate the performance of a RRAM. As indicated in Fig. S5a and b (online), both the single and double memory windows remain stable during ten cycles of triangular wave voltage, illustrating the repeatability of the RRAM behavior. In addition, a high on/off ratio of 10^3 is obtained, which is sufficient to realize the functions of a RRAM (on/off ratio is required to be more than 10) [38]. In addition to the 3-nm-thick mica, similar phenomena (Fig. S6 online) were also observed for ten more devices based on 2D mica with different thicknesses (2–8 nm), and the set voltage positively correlated with the mica thickness. We find that the thicker the mica, the higher the sweep voltage needed to form the CF. To avoid electrical performance variations among samples, more than three mica flakes of each thickness were measured and they exhibited reproducible behavior. Fig. 3e shows the storage time of the graphite/mica/graphite based RRAM after set and reset by a pulse voltage. An obvious resistance difference is observed after measuring the device for over 10^4 s, with a current on/off ratio of around 10^6, indicating that the migration of K$^+$ can retain the accumulated state for a long time. Fig. 3f shows the current of the graphite/mica/graphite device at a read voltage of 5 V after each pulse. The device shows distinct current states during 200 cycles. The set and reset states of the device were achieved by the application of +40 V pulse and –40 V pulse. Furthermore, a device array with 8 × 8 positions in the 2D mica flake was selected (Fig. S7a online). The current of all points in the array was below 10 pA under a read voltage of 1 V, indicating the high uniformity in resistance at the initial state (Fig. S7b online). In comparison, the current increased to a compliance value (10 nA) after the application of a 10 V voltage to set some positions of the array to conductive states. According to the current differences, "T", "B", "S", and "I" patterns were achieved in the array (Fig. 3g). These results show that the mica-based RRAM has high stability, repeatability, reproducibility and multistate storage.

Note that maintaining the state of K$^+$ in mica enables the related device to exhibit the property of a non-Markov chain, which can be
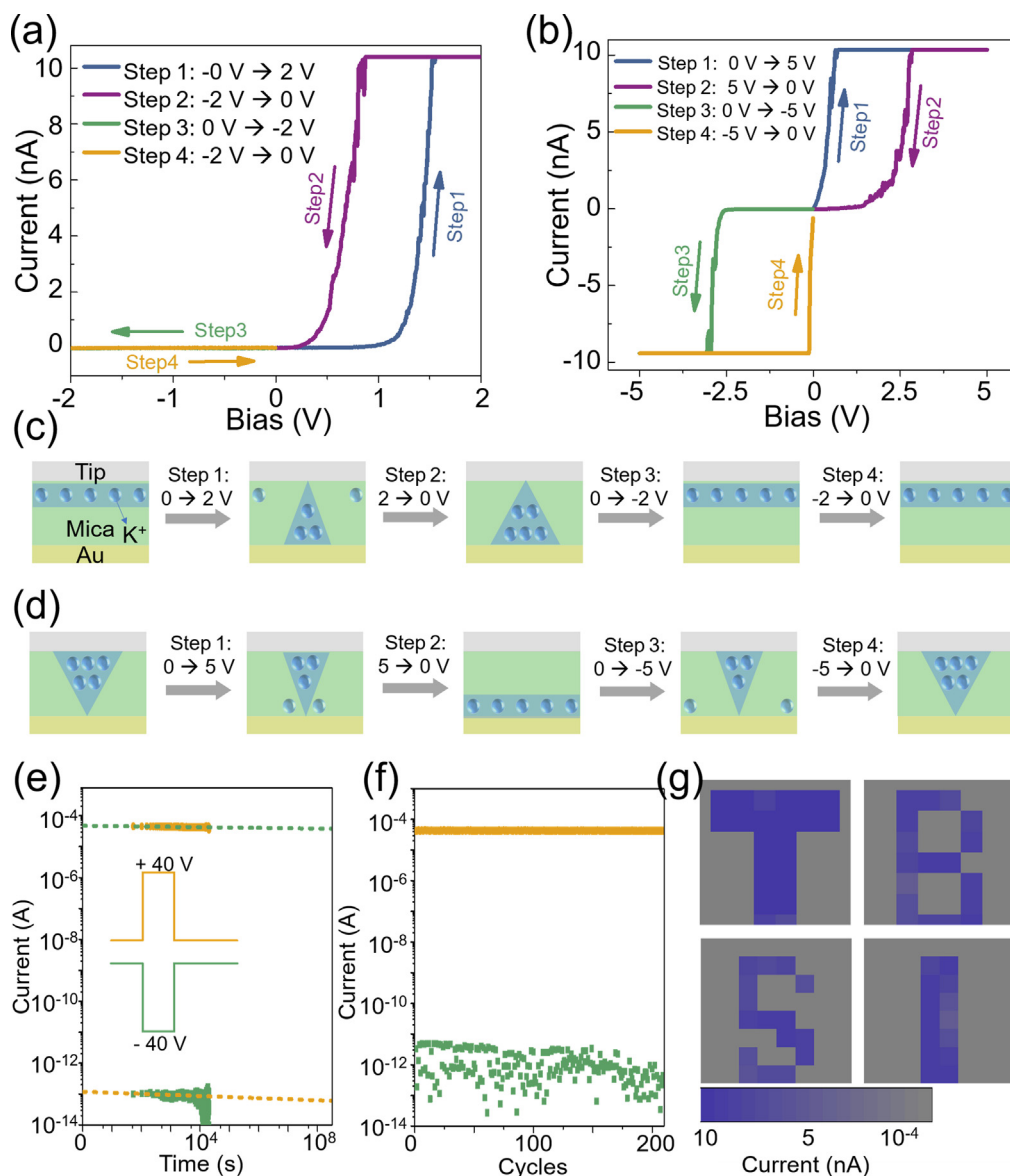
Fig. 3. Electrical performance of the 2D-mica-based RRAM. (a) RRAM behavior of the device at the stimulation of periodic triangular wave voltage with the amplitude of –2 to 2 V. (b) RRAM behavior of the device at the stimulation of periodic triangular wave voltage with the amplitude of –5 to 5 V. Schematic of the accumulation of K^+ in mica under the periodic triangular wave voltage sweep with the amplitude of (c) 2 and (d) 5 V. (e) The current evolution of the set and reset states in the graphite/mica/graphite device. (f) The current distribution of >200 switching cycles in the graphite/mica/graphite device. The current in (e) and (f) were read at a voltage of 5 V. (g) Pattern of a device array with 8 × 8 positions in 2D mica measured under 1 V, in which the composed areas of "T", "B", "S", and "I" patterns are pre-set to be on with a pulse voltage of 10 V.

considered for the relevant applications based on the non-Markov process. The typical non-Markov process can be described as [31]: $P(x_{n+1}=j|x_n=i_n, x_{n-1}=i_{n-1}, x_{n-2}=i_{n-2}, \cdots, x_0=i_0,) \neq P(x_{n+1}=j|x_n=i_n)$, where P is the probability of the states, i, j are the state values, x_{n-1}, $x_{n-2}, \ldots, x_0$ are the past states, x_n is the current state, and x_{n+1} represents the next state of the non-Markov chain. Fig. 4a shows the transfer matrix of a typical non-Markov chain, in which the transfer probability in each state is a function of both current and past states. In our design, three non-Markov states are defined, insulating (State I), high resistance (HR) (State II) and low resistance (LR) (State III), depending on the resistance of the mica-based RRAM. The cartoons in Fig. 4b show parts of the transfer paths of the three states in the device. Positive and negative voltages are applied to stimulate different transformations of states in the non-Markov chain. Two steps of input voltages are applied to initiate the device, in which the first acts as the past transition path while the second serves as the evolution from the current state to the next state, for example, Path 1 (State I → State IIa → State IIIa) and Path 2 (State

I → State IIb → State I), which are illustrated in Fig. 4b. State II is considered as the current state for both paths. Specifically, even at the same state, the K^+ in mica have different memory effects due to their different accumulation pathways induced by the past states. Thus, for the second step, the same positive voltage can switch the device from State IIa to State IIIa or State IIb to State I. This feature suggests that the next state of the system is not only related to the current state, but also to the transport trail of the past states, which is defined as a typical non-Markov process. The experimental results in Fig. 4c show the changing of the resistance of the two examples. Table 1 summarizes all the possible non-Markov paths that can be achieved by the mica-based RRAM. Altogether, by using mica as the RRAM active layer, a non-Markov chain can be realized in a single device. The non-Markov chain has been used in software algorithms. For example, Mikami et al. [39] demonstrated the memory based non-Markov strategy for face pose tracking of abrupt object movements in complex dynamics, where they stored the total past state history of the target and used
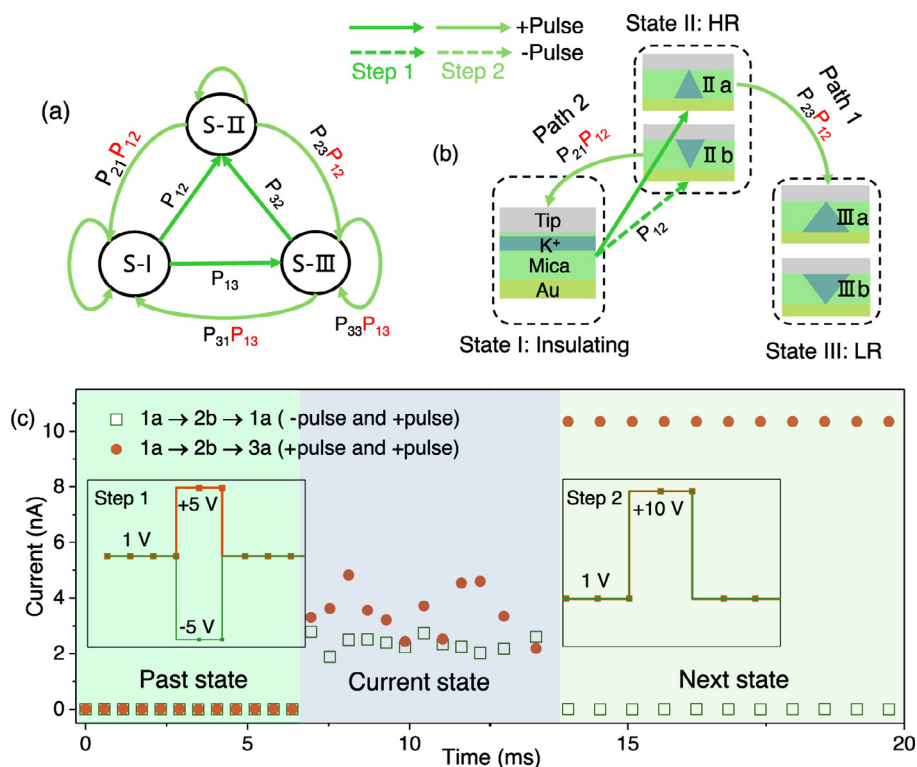
Fig. 4. Realization of a non-Markov chain in a single RRAM. Schematics of (a) a typical non-Markov process and (b) a non-Markov chain achieved by a mica-based device. The three resistance states of the device are defined as State I, State II, and State III, which correspond to insulating, HR and LR states, respectively. The applied positive and negative pulse voltages are indicated by solid and dotted arrows, respectively. The first and second step of the state transformation are represented by green and orange arrows, respectively. Examples of the non-Markov process by following the paths of (c) State I → State IIa → State IIIa and State I → State IIb → State I.

Table 1
Realization of all possible non-Markov paths in a single mica-based RRAM.

Comparison of two non-Markov paths	Input voltages (V)
Path 1: I → IIa → IIIa, Path 2: I → IIb → I	5 → 10, −5 → 10
Path 1: I → IIa → I, Path 2: I → IIb → IIIa	5 → −10, −5 → −10
Path 1: I → IIIa → IIIa, Path 2: I → IIIb → I	10 → 10, −10 → 10
Path 1: I → IIIa → I, Path 2: I → IIIb → IIIb	10 → −10, −10 → −10

it to generate an accurate prior distribution of state. In another study using a non-Markov model, Peng et al. [40] studied the future credit rating of companies according to the rating of the present and previous quarters, which is particularly useful in areas that traditional Markov model cannot deal with due to sample size limits. Note that many of these studies are software algorithm based. We think it is meaningful to realize these non-Markov functions using hardware devices because it can evaluate the effectiveness of the algorithm. The integration of the 2D-mica-based RRAM arrays with non-Markov characteristics is expected to simulate these complex processes in future. Note that in the current work the RS behavior and non-Markov chain are realized in a single mica flake, which is not suitable for industrial applications. We envision that using the top-down exfoliation [41,42] and film assembly techniques would facilitate the scalable fabrication of mica films or films made of other ionic conductive layered 2D mineral materials for such devices.

4. Conclusion

We have achieved a non-Markov chain in a single 2D crystal RRAM. The conductive mechanism of the device is related to the vertical migration of K^+ in the 2D mineral mica under an electric field, which has been verified by both electrical transport characterization and depth profiling with TOF-SIMS analysis. The accumulated K^+ shows distinct behaviors under electrical fields in opposite directions, resulting in a combination of single and double RRAM windows of a 2D mica RRAM. Note that the 2D mica-based RRAM uses inner ions for conduction, which is different with other reports [19–21,23]. The device has a high on/off ratio of 10^3, good repeatability, and decent reliability. The realization of a non-Markov chain in a single device opens a new horizon in highly-efficient and integrated systems for future in-memory computing and intelligent devices.

Conflict of interest

The authors declare that they have no conflict of interest.

Author contributions

Hui-Ming Cheng and Bilu Liu conceived the idea and supervised the project. Rongjie Zhang fabricated the devices and performed CAFM measurements with Wenjun Chen. Wenjun Chen and Wugang Liao helped analyze the transport of inner ions in 2D mica. Rongjie Zhang and Changjiu Teng carried out the analysis of non-Markov chain. Rongjie Zhang, Wenjun Chen, Bilu Liu, and Hui-Ming Cheng wrote the manuscript with revisions and feedbacks from other authors.

Appendix A. Supplementary materials

Supplementary materials to this article can be found online at https://doi.org/10.1016/j.scib.2021.04.025.

References

[1] Backus J. Can programming be liberated from the von Neumann style? A functional style and its Algebra of programs. Commun ACM 1978;21:613–41.

[2] Srikanth S, Conte TM, DeBenedictis EP, et al. The superstrider architecture: integrating logic and memory towards non-von Neumann computing. 2017 IEEE Int Conf Rebooting Comput ICRC 2017 - Proc 2017:1–8.

[3] Wu H, Yao P, Gao B, et al. Multiplication on the edge. Nat Electron 2018;1:8–9.

[4] Di Ventra M, Pershin YV. The parallel approach. Nat Phys 2013;9:200–2.

[5] Zhang Y, Qu P, Ji Y, et al. A system hierarchy for brain-inspired computing. Nature 2020;586:378–84.

[6] Chua L. Memristor—the missing circuit element. IEEE Trans Circuit Theory 1971;18:507–19.

[7] Strukov DB, Snider GS, Stewart DR, et al. The missing memristor found. Nature 2008;453:80–3.

[8] Yang JJ, Strukov DB, Stewart DR. Memristive devices for computing. Nat Nanotechnol 2013;8:13–24.

[9] Zhang Z, Wang Z, Shi T, et al. Memory materials and devices: from concept to application. InfoMat 2020;2:261–90.

[10] Indiveri G, Liu S-C. Memory and information processing in neuromorphic systems. Proc IEEE 2015;103:1379–97.

[11] Zhang W, Gao B, Tang J, et al. Neuro-inspired computing chips. Nat Electron 2020;3:371–82.

[12] Tran MD, Kim H, Kim JS, et al. Two-terminal multibit optical memory via van der Waals heterostructure. Adv Mater 2019;31:7.

[13] Wang CY, Wang C, Meng F, et al. 2D layered materials for memristive and neuromorphic applications. Adv Electron Mater 2020;6:1–22.

[14] Zhao Q, Xie Z, Peng Y-P, et al. Current status and prospects of memristors based on novel 2D materials. Mater Horizons 2020;7:1495–518.

[15] Zhang L, Gong T, Wang H, et al. Memristive devices based on emerging two-dimensional materials beyond graphene. Nanoscale 2019;11:12413–35.

[16] Liu C, Chen H, Wang S, et al. Two-dimensional materials for next-generation computing technologies. Nat Nanotechnol 2020;15:545–57.

[17] Migliato Marega G, Zhao Y, Avsar A, et al. Logic-in-memory based on an atomically thin semiconductor. Nature 2020;587:72–7.

[18] Zhang F, Zhang H, Shrestha PR, et al. An ultra-fast multi-level $MoTe_2$-based RRAM. 2018 IEEE Int Electron Devices Meet. IEEE; 2018. p. 22.7.1-22.7.4.

[19] Wu X, Ge R, Chen P-A, et al. Thinnest nonvolatile memory based on monolayer h-BN. Adv Mater 2019;31:1806790.

[20] Zhao H, Dong Z, Tian H, et al. Atomically thin femtojoule memristive device. Adv Mater 2017;29:1703232.

[21] Xu R, Jang H, Lee M-H, et al. Vertical MoS_2 double-layer memristor with electrochemical metallization as an atomic-scale synapse with switching thresholds approaching 100 mV. Nano Lett 2019;19:2411–7.

[22] Kim M, Ge R, Wu X, et al. Zero-static power radio-frequency switches based on MoS_2 atomristors. Nat Commun 2018;9:2524.

[23] Wang M, Cai S, Pan C, et al. Robust memristors based on layered two-dimensional materials. Nat Electron 2018;1:130–6.

[24] Silver D, Huang A, Maddison CJ, et al. Mastering the game of Go with deep neural networks and tree search. Nature 2016;529:484–9.

[25] Yao P, Wu H, Gao B, et al. Face classification using electronic synapses. Nat Commun 2017;8:15199.

[26] Prezioso M, Merrikh-Bayat F, Hoskins BD. Training and operation of an integrated neuromorphic network based on metal-oxide memristors. Nature 2015;521:61–4.

[27] Zhou F, Zhou Z, Chen J, et al. Optoelectronic resistive random access memory for neuromorphic vision sensors. Nat Nanotechnol 2019;14:776–82.

[28] Li C, Hu M, Li Y, et al. Analogue signal and image processing with large memristor crossbars. Nat Electron 2018;1:52–9.

[29] Yao P, Wu H, Gao B, et al. Fully hardware-implemented memristor convolutional neural network. Nature 2020;577:641–6.

[30] Mennel L, Symonowicz J, Wachter S, et al. Ultrafast machine vision with 2D material neural network image sensors. Nature 2020;579:62–6.

[31] Tian H, Wang X-F, Mohammad MA, et al. A hardware Markov chain algorithm realized in a single device for machine learning. Nat Commun 2018;9:4305.

[32] Hanggi P, Thomas H. Time evolution, correlations, and linear response of non-Markov processes. Zeitschrift Für Phys B Condens Matter Quanta 1977;26:85–92.

[33] Shabani A, Roden J, Whaley KB. Continuous measurement of a non-Markovian open quantum system. Phys Rev Lett 2014;112:23–8.

[34] Huang CY, Shen WC, Tseng YH, et al. A contact-resistive random-access-memory-based true random number generator. IEEE Electron Device Lett 2012;33:1108–10.

[35] Balatti S, Ambrogio S, Wang Z, et al. True random number generation by variability of resistive switching in oxide-based devices. IEEE J Emerg Sel Top Circuits Syst 2015;5:214–21.

[36] Harvey SP, Messinger J, Zhu K, et al. Investigating the effects of chemical gradients on performance and reliability within perovskite solar cells with TOF-SIMS. Adv Energy Mater 2020;10:1903674.

[37] Nguyen VS, Mai VH, Auban Senzier P, et al. Direct evidence of lithium ion migration in resistive switching of lithium cobalt oxide nanobatteries. Small 2018;14:1801038.

[38] Chen A, Lin M-R. Variability of resistive switching memories and its impact on crossbar array performance. 2011 Int Reliab Phys Symp. IEEE; 2011. p. MY.7.1-MY.7.4.

[39] Mikami D, Otsuka K, Yamato J. Memory-based particle filter for face pose tracking robust under complex dynamics. IEEE Conf Comput Vis Pattern Recognit 2009:999–1006.

[40] Peng GC, Hin PA, Haur NK. Prediction of future credit rating using a non-Markovian model. AIP Conf Proc 2017:080002.

[41] Zhang C, Tan J, Pan Y, et al. Mass production of 2D materials by intermediate-assisted grinding exfoliation. Natl Sci Rev 2020;7:324–32.

[42] Zhang C, Luo Y, Tan J, et al. High-throughput production of cheap mineral-based two-dimensional electrocatalysts for high-current-density hydrogen evolution. Nat Commun 2020;11:3724.

Rongjie Zhang received his bachelor's and master's degrees from Fuzhou University in 2016 and Tianjin University in 2019, respectively. He is a Ph.D. student at the Low-Dimensional Materials and Devices Laboratory, Tsinghua-Berkeley Shenzhen Institute (TBSI), Tsinghua University. His research interest focuses on electronic and optoelectronic devices based on two-dimensional materials, including FETs, memristors, and sensors.

Wenjun Chen obtained his Ph.D. degree from Sun Yat-sen University in 2018 and worked as a postdoctoral fellow at TBSI, Tsinghua University from 2018 to 2020. Afterwards, he joined Foshan University in 2021. His research interest focuses on the 2D materials, their physical properties, and applications in flexible electronics.

Bilu Liu is an associate professor and a principal investigator at TBSI, Tsinghua University. His research interest covers the chemistry and materials science of low-dimensional materials with an emphasis on carbon nanostructures, 2D materials, and their heterostructures. His work relates to the controlled preparation of these materials and their applications in electronics, optoelectronics, and catalysis.

Hui-Ming Cheng is a professor of the Advanced Carbon Research Division at Shenyang National Laboratory for Materials Science, Institute of Metal Research, Chinese Academy of Sciences, and also the Low-Dimensional Materials and Devices Laboratory, TBSI, Tsinghua University. His research interest is focused on the synthesis and applications of carbon nanotubes, graphene, other 2D materials, and high-performance bulk carbons, and on the development of new energy materials for batteries, electrochemical capacitors, and hydrogen production from water by photocatalysis.